The Astrophysical Journal, 908:62 (14pp), 2021 February 10 https://doi.org/10.3847/1538-4357/abd320

Mapping the Supernovae Driven Winds of the Large Magellanic Cloud in Hα Emission I

Drew A. Ciampa[1], Kathleen A. Barger[1], Nicolas Lehner[2], Madeline Horn[1,3], Michael Hernandez[1], L. Matthew Haffner[4,5,6], Brianna Smart[6,7], Chad Bustard[8], Sam Barber[1,9], and Henry Boot[1,10]
[1] Department of Physics & Astronomy, Texas Christian University, Fort Worth, TX 76129, USA; drew.ciampa@tcu.edu
[2] Department of Physics, University of Notre Dame, Notre Dame, IN 46556, USA
[3] Department of Astronomy, Smith College, Northampton, MA 01063, USA
[4] Embry-Riddle Aeronautical University, Daytona Beach, FL 32114, USA
[5] Space Science Institute, Boulder, CO 80301, USA
[6] Department of Astronomy, University of Wisconsin-Madison, Madison, WI 53706, USA
[7] Department of Physics, Astronomy, and Mathematics, University of Hertfordshire, Hatfield AL10 9AB, UK
[8] Department of Physics, University of Wisconsin-Madison, Madison, WI 53706, USA
[9] Trinity Valley High School, Fort Worth, TX 76132, USA
[10] Burleson High School, Burleson, TX 76028, USA
Received 2020 February 19; revised 2020 December 10; accepted 2020 December 10; published 2021 February 15

Abstract

We present the first spectroscopically resolved Hα emission map of the Large Magellanic Cloud's (LMC) galactic wind. By combining new Wisconsin H-alpha Mapper observations ($I_{\mathrm{H}\alpha} \gtrsim 10$ mR) with existing H I 21 cm emission observations, we (1) mapped the LMC's nearside galactic wind over a local standard of rest (LSR) velocity range of $+50 \leqslant v_{\mathrm{LSR}} \leqslant +250$ km s^{-1}, (2) determined its morphology and extent, and (3) estimated its mass, outflow rate, and mass-loading factor. We observe Hα emission from this wind to typically 1° off the LMC's H I disk. Kinematically, we find that the diffuse gas in the warm-ionized phase of this wind persists at both low ($\lesssim$100 km s^{-1}) and high ($\gtrsim$100 km s^{-1}) velocities, relative to the LMC's H I disk. Furthermore, we find that the high-velocity component spatially aligns with the most intense star-forming region, 30 Doradus. We, therefore, conclude that this high-velocity material traces an active outflow. We estimate the mass of the warm ($T_e \approx 10^4$ K) ionized phase of the nearside LMC outflow to be $\log(M_{\mathrm{ionized}}/M_\odot) = 7.51 \pm 0.15$ for the combined low and high-velocity components. Assuming an ionization fraction of 75% and that the wind is symmetrical about the LMC disk, we estimate that its total (neutral and ionized) mass is $\log(M_{\mathrm{total}}/M_\odot) = 7.93$, its mass-flow rate is $\dot{M}_{\mathrm{outflow}} \approx 1.43\ M_\odot$ yr^{-1}, and its mass-loading factor is $\eta \approx 4.54$. Our average mass-loading factor results are roughly a factor of 2.5 larger than previous Hα imaging and UV absorption line studies, suggesting that those studies are missing nearly half the gas in the outflows.

Unified Astronomy Thesaurus concepts: Dwarf galaxies (416); Galaxy evolution (594); Interstellar medium (847); Large Magellanic Cloud (903); Circumgalactic medium (1879); High-velocity clouds (735); Galactic winds (572); Stellar feedback (1602)

1. Introduction

Galactic feedback, such as stellar winds, supernovae, and active galactic nuclei, expel both energy and momentum into the interstellar medium (ISM) of the host galaxy. These processes can further drive gas out of the galaxies in galactic winds and fountains. As these processes cycle gaseous material through the galaxy and into its surroundings, they transport enriched gas to the outskirts of the galaxy and into the circumgalactic medium (CGM; Heckman 2003; Veilleux et al. 2005; Tumlinson et al. 2011). Furthermore, if the gas that is ejected into the CGM is lost from the galaxy or if it stagnates into the galaxy's halo (e.g., Ford et al. 2014; Peeples et al. 2014), the star formation rate of the galaxy will likely decline unless it is able to procure additional gaseous material from different sources. In most cases, this baryon cycle is difficult to resolve because the gaseous material in the ISM and CGM is faint. However, the nearby Large Magellanic Cloud (LMC) provides an unparalleled view of gaseous material both within and surrounding its disk. By investigating the gaseous material in the CGM of the LMC, we can better understand its behavior, enabling us to decipher how the baryon cycle is connected to galaxy evolution.

At a distance of about $d_\odot \approx 50$ kpc (Walker 1999; Pietrzyński et al. 2013; de Grijs et al. 2014), the LMC is close enough to resolve spatial features within its ISM. The stellar and total mass, $M_\star = 3 \times 10^9\ M_\odot$ (van der Marel et al. 2009) and $M_{\mathrm{total}} = 1.7 \times 10^{10}\ M_\odot$ ($r_{\mathrm{enclosed}} = 8.7$ kpc; van der Marel & Kallivayalil 2014), make the LMC a low-mass galaxy allowing gas to interact more freely with its environment and distribute material with the CGM efficiently (Heckman et al. 2000). The gaseous disk of this galaxy is projected nearly face-on with an inclination angle of $22° \lesssim i \lesssim 26°$ (Kim et al. 1998; Staveley-Smith et al. 2003; Choi et al. 2018), providing an unobstructed view of its ISM and activity within the disk. Observations have shown numerous neutral hydrogen super shells and holes that exist throughout the LMC's (Meaburn 1980; Kim et al. 1999), which could be a result of interactions with the Small Magellanic Cloud (SMC) and possibly the Milky Way (MW; e.g., Besla et al. 2010, 2012), as well as recent periods of intense star formation due to its interaction with the SMC (Harris & Zaritsky 2009). Each of these studies suggests an active history and stellar lifecycle that could lead to outflows with large amounts of energy and material blown into their surroundings during times of increased stellar activity (Erb 2015). The addition of energy and momentum from numerous supernovae throughout the galaxy could be a way for a large-scale outflow to originate in a galaxy like the LMC. Observations capturing a complete picture of any galactic-wide outflowing material proved difficult due to

the LMC's size on the sky. Observations of the Hα emission from the ISM of the LMC in prior studies focused primarily inside the LMC's disk (Rosado et al. 1990, Laval et al. 1992, and Reid & Parker 2012). While these studies revealed activity within the ISM of the LMC (Pellegrini et al. 2012 and Winkler et al. 2015), they only observed the brighter inner region of the LMC rather than the faint emission from its extended diffuse disk and the galaxy's CGM.

Although the LMC is our nearest gas-rich neighboring galaxy, it was not until recently that many studies began to directly detect signatures of a large-scale galactic outflow. Recent ultraviolet (UV) absorption-line spectroscopy studies, using the Hubble Space Telescope and Far Ultraviolet Spectroscopic Explorer, investigated gas flows of the LMC (Howk et al. 2002; Lehner & Howk 2007; Lehner et al. 2009; Pathak et al. 2011). Howk et al. (2002) used 12 stars embedded within the LMC as background targets to explore the gas on the nearside of the LMC; they found that the absorption along every sightline had kinematic signatures consistent with gaseous material flowing out of the LMC. A study performed by Staveley-Smith et al. (2003) using the H I 21 cm emission-line surveyed found high-velocity clouds (HVCs) in the direction of the LMC and kinematic and morphological evidence that these clouds could be associated with an LMC galactic outflow. A subsequent absorption-line investigation conducted by Lehner & Howk (2007) toward four more LMC stars confirmed the presence of outflowing gas and further found that the LMC's gas outflows correlated with H II regions and super shells, possibly signaling they are a result of supernovae in the disk. The blueshifted material, relative to the LMC, was also detected along sightlines that projected onto relatively quiescent regions. Lying in the direction of the LMC, Lehner et al. (2009) found further evidence that the HVC may have originated from an earlier LMC outflow event. They observed that this cloud has a velocity gradient with R.A. in H I emission and low-ionization species (see their Figure 5), a similar oxygen abundance as the LMC, and depletion patterns that indicate the presence of dust—a strong indicator that this material is of LMC origin.

However, Werner & Rauch (2015) were able to determine an upper distance limit of an HVC at a similar velocity that is positioned only a few degrees offset from the LMC's disk using absorption-line spectroscopy toward a halo star at a known distance. They found the cloud along $(l,\ b) = (279.9°, -37.1°)$ only lies $d_{\odot} \lesssim 13.3$ kpc away. While their distance limit provides compelling evidence that some of the HVC material at a local standard of rest (LSR) velocity of $v_{LSR} = 150\ km\ s^{-1}$ is likely of MW origin (Richter et al. 2015), this does not eliminate the possibility of two separate HVC complexes. It remains that toward the LMC, an HVC is observed where the H I position–velocity map shows a physical association with the LMC (Staveley-Smith et al. 2003), not the MW. It is one of the sole HVCs where dust depletion is observed (Lehner et al. 2009). The occurrence of both an MW and LMC HVC around the same projected area is plausible given the prior work and the large angular region being explored.

Each of the previously mentioned absorption-line studies that detected blueshifted material in the direction of the LMC use background targets embedded within the disk of the LMC, which only traces material between the MW and LMC. Moreover, the majority of previously explored sightlines were preferentially selected toward active star formation regions where outflows are more likely to occur. However, there are four locations in Lehner & Howk (2007) that probe relatively quiescent regions that still find blueshifted material relative to the LMC, leaving open the possibility of a galactic wind across the nearside of the LMC disk. This comes in addition to the prospect of a hot corona coexisting with the wind (de Boer & Savage 1980; Wakker et al. 1998; Lucchini et al. 2020). The scenario of both an outflow and corona would support itself in that the outflow may feed the corona and supply it with gas.

In order to probe gas flows on the farside of the LMC, Barger et al. (2016) used a "down-the-barrel" (star) and transverse (quasi-stellar object (QSO)) experiment to isolate material that is located on the farside of the LMC disk. They found that both the low and high ions are symmetrically flowing out of the LMC disk at speeds representing an intermediate-velocity cloud (IVC). Those results, when combined with the previous studies of Howk et al. (2002) (absorption from 12 LMC stars showing outflowing material), Lehner & Howk (2007) (additional four LMC stars correlating with H II bubbles and super shells), Lehner et al. (2009) (gradient found in the HVC toward the LMC), and Pathak et al. (2011) (strong absorption in O VI across the entire face of the LMC), provide convincing evidence that the LMC drives a global, large-scale outflow across its entire disk.

Our study supplements the previous UV work by supplying the first spectroscopically resolved Hα map of the LMC and its surrounding environment. This approach removes limitations of previous works that had small numbers of pointings that were dependent on the location of background targets, which severely reduced the spatial coverage of the material they observed. The work we present is unique in that (1) our observations are roughly an order of magnitude more sensitive than previous studies—enabling us to map the diffuse optical emission from these clouds—and that (2) we were able to spatially resolve the entirety of the LMC and its surroundings at an angular resolution of $\theta_{resolution} = 1°$. Both of these results cannot be performed with the vast majority of other more distant gas-rich galaxies. With emission-line observations of the ionized component of the LMC's IVCs and HVCs, we explore their global morphology and kinematic distribution in Section 5. In this section, we further assess whether the IVC material could be associated with an LMC wind origin. In Section 6, we discuss how a portion of the emission is from gas currently being driven from the galaxy as an IVC. This is followed up with an estimate of this material's mass as well as it is role in the LMC's neighborhood (Sections 6.1 and 6.2). Section 7 discusses an HVC that is moving at speeds upward of $\Delta v_{LMCSR} \approx -150\ km\ s^{-1}$. The significance and possible explanation for this material's origin is considered in Section 7.1.

2. Data

This study utilizes archival radio and newly acquired optical emission-line observations to trace the neutral and ionized hydrogen gas in and around the LMC.

2.1. Wisconsin Hα Mapper (WHAM)

We surveyed the faint Hα ($\lambda_{H\alpha} = 6562.8$ Å) emission across the face of the LMC's disk and in the region that surrounds it

using the WHAM telescope over the $+50 \leqslant v_{\rm LSR} \leqslant +250\,{\rm km\,s^{-1}}$ velocity range.[11] Equipped with a Fabry–Pérot spectrometer, WHAM is roughly an order of magnitude more sensitive than other currently available instruments, enabling us to detect the faint emission at a sensitivity limit of $I_{\rm H\alpha} \approx 10\,{\rm mR}$[12] per 30 s exposure. WHAM's sensitivity is achieved due to its high throughput resulting from its 1° beam size. By adjusting the gas pressures between the instruments etalon, we can tune our observations to center on the Hα emission line that is associated with the LMC. More information about the WHAM telescope and its capabilities are outlined in Haffner et al. (2003).

Our WHAM observations have a $\theta_{\rm resolution} = 1^\circ$ angular resolution, which corresponds to a $\Delta d_{\rm resolution} \approx 1$ kpc spatial resolution at the distance of the LMC. The observations were Nyquist sampled across the face of the galaxy, effectively increasing the integration time per location on the sky and removing gaps between observations with overlapping pointings. Our Hα survey contains more than 6600 individual observations that are positioned both on and off the LMC's H I disk, covering an area that spans from $(l, b) = (246.5^\circ, -17.8^\circ)$ to $(315.0^\circ, -46.7^\circ)$.

2.2. Radio Data

We use archival H I 21 cm emission-line data from the Parkes Galactic All-Sky Survey (GASS;[13] McClure-Griffiths+2009) to probe the neutral hydrogen gas phase in the LMC at an angular resolution of $\theta_{\rm resolution} = 16'$, corresponding to an angular area that is roughly 14 × smaller than that of the WHAM beam. This survey spans a velocity range of $-400 \leqslant v_{\rm LSR} \leqslant +500\,{\rm km\,s^{-1}}$ and has a spectral resolution of $\Delta v_{\rm resolution} = 0.82\,{\rm km\,s^{-1}}$. The rms brightness temperature noise is $T_{\rm B,\ RMS} = 57$ mK, corresponding to a 3σ sensitivity of $\log(N_{\rm H\,I}/\,{\rm cm^{-2}}) \approx 18.2$ for a typical high-velocity cloud line width of $30\,{\rm km\,s^{-1}}$ (McClure-Griffiths et al. 2009).[14] In this paper, the survey's 3σ limit is far lower than the practical limit used for our maps and mass calculation.

In addition to the GASS data, we use a combined H I 21 cm emission-line map consisting of combined Australia Telescope Compact Array (ATCA) and Parkes telescope observations (Kim et al. 2003). The velocity range of this LMC H I survey spans $+190 \leqslant v_{\rm LSR} \leqslant +375\,{\rm km\,s^{-1}}$ and has a $\Delta v_{\rm resolution} = 1.6\,{\rm km\,s^{-1}}$ spectral resolution. Compared to the GASS survey, this combined map has a column density sensitivity of $\log(N_{\rm H\,I}/\,{\rm cm^{-2}}) \approx 18.86$ for a $\Delta v = 30\,{\rm km\,s^{-1}}$ wide line, but a much higher spatial resolution at $\theta_{\rm resolution} = 1'$. This data resolves smaller physical structures than GASS, improving our ability to discern smaller-scale morphological features in the disk.

We also use data from the Leiden/Argentine/Bonn (LAB) Survey to measure extinction along our sightlines due to its similar beam size as WHAM. LAB data has an effective FWHM beam of $\theta_{\rm resolution} = 35'$ for decl. $\leqslant -27^\circ$. The survey covers a velocity range of $-450 \leqslant v_{\rm LSR} \leqslant +400\,{\rm km\,s^{-1}}$ with a spectral resolution of $\Delta v_{\rm resolution} = 1.3\,{\rm km\,s^{-1}}$. The rms noise is $T_{\rm B,rms} = 0.07$ K resulting in a 3σ sensitivity of $\log(N_{\rm H\,I}/\,{\rm cm^{-2}}) \approx 18.38$.

3. Data Reduction

The Hα reduction process we performed was carried out in two stages. In the first stage, we used the standard WHAM reduction pipeline, which performs the bias subtraction, flat-fielding, ring-summing, cosmic-ray contamination removal, and air mass corrections. In the second stage, we velocity calibrated our spectra, removed atmospheric signatures from observations, masked out observations affected by foreground stars, and corrected for dust extinction.

3.1. WHAM Pipeline

We utilized the WHAM pipeline that is described in detail in Haffner et al. (2003). During this data processing, pixels warmed by cosmic rays were first removed. The circular interference patterns that result from our Fabry–Pérot spectrometer observations were summed in annuli to produce a linear spectrum that is a function of velocity. These linear spectra span a $\Delta v = 200\,{\rm km\,s^{-1}}$ velocity range and are uniformly binned to $\Delta v_{\rm bin} = 2\,{\rm km\,s^{-1}}$ intervals. The pipeline normalizes the spectra by exposure time, scales them for the air mass of observations, and applies an intensity correction factor to account for sensitivity degradation of the WHAM instrumentation that occurs over time.

3.2. Velocity Calibration

Our observations span $+50 \leqslant v_{\rm GEO} \leqslant +250\,{\rm km\,s^{-1}}$ in the geocentric (GEO) velocity frame. Over this range, these observations do not overlap with the bright geocoronal Hα line at $v_{\rm GEO} = -2.3\,{\rm km\,s^{-1}}$ and only overlaps with the blue wing of a bright OH line at $v_{\rm GEO} = +272.44\,{\rm km\,s^{-1}}$. Therefore, we were unable to use either of these lines to calibrate our velocities using the method described in Hausen et al. (2002) and Barger et al. (2013). Instead, we used the velocity calibration technique that is described by Barger et al. (2017) and Antwi-Danso et al. (2020) for WHAM observations that do not overlap with bright atmospheric lines at well established transitions. Using this technique, we calibrated our velocity by monitoring the pressure of the SF_6 gas in the WHAM Fabry–Pérot etalons and by further refining the calibration by comparing our observations with an atmospheric template.

Using the linear relationship between the pressure of the Fabry–Pérot etalons and $\Delta\lambda$ measured by Tufte (1997), we calculated the velocity offset between the raw and GEO velocity frames. This is essentially the reverse of our tuning process, which enabled us to calibrate the velocity frame to an accuracy of $\Delta v_{\rm GEO} \lesssim 5\,{\rm km\,s^{-1}}$. Because all of our observations were taken at the same tune (i.e., at the same interference order), the relative velocities of the calibrated observations agree within $0.1\,{\rm km\,s^{-1}}$ of each other as described in Barger et al. (2017). We improved our calibration further by aligning our observations with the faint atmospheric lines in the atmospheric template presented by Barger et al. (2013) (see their Figure 3). This enabled our velocity solution to be calibrated to an accuracy of $\Delta v_{\rm GEO} \lesssim 1\,{\rm km\,s^{-1}}$. We then

[11] We use the kinematic definition of the LSR in which the Sun moves $20\,{\rm km\,s^{-1}}$ in the direction of (R.A., decl.) = ($18^{\rm h}3^{\rm m}50\overset{\rm s}{.}29$, $30^\circ00'16\overset{''}{.}8$) for the Julian 2000 epoch (J2000).

[12] A Rayleigh (R) is a unit of measure for the surface brightness of emission lines that is equal to $1\,{\rm R} = 10^6/4\pi$ photons cm^{-2} sr^{-1} s^{-1}, which is 5.6×10^{-18} erg s^{-1} cm^{-2} arcsec^{-2} for Hα.

[13] The GASS survey is a publicly available survey with access through an online database retrieval site: https://www.atnf.csiro.au/research/GASS/Data.html.

[14] We convert H I brightness temperatures ($T_{\rm B}$) to column densities using the relationship $N_{\rm H\,I} = 1.823 \times 10^{18} \int (T_{\rm B}/{\rm K})(dv/{\rm km\,s^{-1}})\,{\rm cm^{-2}}$, which assumes that these clouds optically thin 21 cm radiation.

converted from GEO to LSR using a constant offset that accounted for the date, time, and location of each observation.

3.3. Atmospheric Subtraction

3.3.1. Atmospheric Template

There are significant faint atmospheric emission features that populate the entire velocity range of our observations. While these lines are abundant, they behave predictably and vary primarily with air mass. Because of this, we modeled these lines using a template created by Barger et al. (2013) (see their Figure 3), which characterizes the atmospheric emission present in our observations. The template was scaled to account for differences in air mass between observations and night-to-night variations due to humidity and temperature.

Brighter lines are more variable and need to be fit individually. This includes a bright OH molecular line at $v_{\rm GEO} = 272.44\ {\rm km\ s^{-1}}$ whose line strength depends on the angle between the Sun and Earth's upper atmosphere. In the direction of the LMC, this bright OH line is overwhelmed by emission from the LMC's disk. To subtract this emission feature in the direction of the LMC, we kept the area and width of the line fit constant so that it matched with off-disk observations that were taken during the same night and within roughly 15 minutes of the on-disk observations. Because this narrow OH line is kinematically unresolved by the WHAM telescope, we fit the line assuming that it has a width of $\Delta v_{\rm OH\ width} = 1\ {\rm km\ s^{-1}}$ before we convolved it with WHAM's $\Delta v_{\rm WHAM\ IP} \approx 12\ {\rm km\ s^{-1}}$ instrument profile.

We fit the background emission with a constant term added to the atmospheric template. The total fit—which includes the bright OH line at $v_{\rm geo} = 272.44\ {\rm km\ s^{-1}}$, faint atmospheric lines, a flat background, and Gaussian modeled astronomical emission—utilized a chi-square minimization with conservative criteria to avoid over-fitting emission features that are not physically realistic. These criteria account for the line width and lower limits for the strength of the astronomical emission, which are dependent on the gas temperature and instrument sensitivity, respectively. An example of the pre- and post-atmospheric corrected spectrum is shown in Figure 1 with a sightline piercing through the LMC. A detailed description of these bright lines and how they were handled, including their origin and the nature of their variability, is outlined in Barger et al. (2013).

3.3.2. Removal of Systematic Signatures

Following the removal of the atmospheric contamination with the atmospheric template described above, we discovered systematic spectral signatures in the reduced spectra. The cause of these structured residuals is likely due to very faint, unresolved atmospheric lines that are not described in the atmospheric template or from a slight velocity misalignment between the observed spectra and the atmospheric template causing the signatures during subtraction. These signatures appear at the same GEO rest-frame velocity over narrow, $5 \lesssim \Delta v \lesssim 10\ {\rm km\ s^{-1}}$, velocity widths. These signatures are visible when the spectra in our survey are stacked across the same velocity range in the GEO frame, as shown in the top panel of Figure 2. At several velocities in this frame, there are multiple relatively coherent vertical signatures across the spectra. However, the two bright astronomical horizontal structures are associated with the Magellanic Bridge (MB)

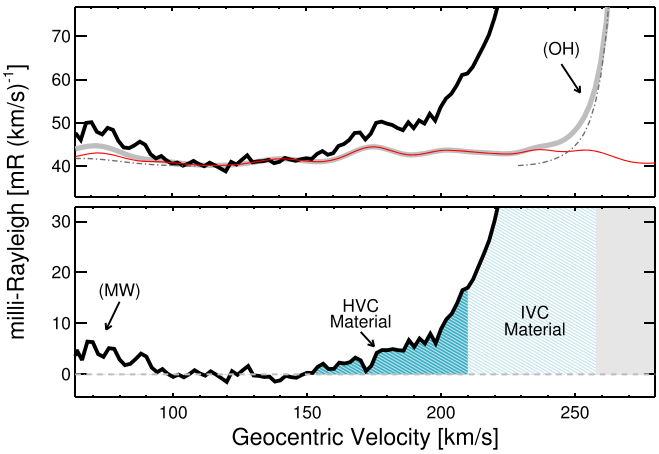

Figure 1. (Top panel) A pre-atmospheric subtracted WHAM spectrum toward $(l,\ b) = (279.0°,\ -31.0°)$ drawn as the black line. The atmospheric template we used to reduce our Hα observations is indicated with a red overlaid line. The emission contributions associated with the MW at $v_{\rm GEO} = +66.21\ {\rm km\ s^{-1}}$ and a bright OH line at a velocity of $v_{\rm GEO} = +272.44\ {\rm km\ s^{-1}}$ are traced with dashed–dotted gray lines. The solid, thick gray line traces all of the atmospheric emission (atmospheric template and OH line) that we subtracted from the WHAM spectrum during our reduction procedure. (Bottom panel) The final reduced spectrum, where emission from the LMC ($v_{\rm GEO} \gtrsim +260\ {\rm km\ s^{-1}}$) is shaded light gray, LMC IVC material ($+210 \lesssim v_{\rm GEO} \lesssim +260\ {\rm km\ s^{-1}}$) is shaded light blue, LMC HVC material ($+150 \lesssim v_{\rm GEO} \lesssim +210\ {\rm km\ s^{-1}}$) is shaded dark blue, and the MW ($v_{\rm GEO} \lesssim +90\ {\rm km\ s^{-1}}$) is marked.

($+150 \lesssim v_{\rm GEO} \lesssim +210\ {\rm km\ s^{-1}}$ and $0 \leqslant$ spectrum channel $\leqslant 35$) and the LMC and its wind ($+150 \lesssim v_{\rm GEO} \lesssim +300\ {\rm km\ s^{-1}}$ and $100 \leqslant$ spectrum channel $\leqslant 200$).

These faint residual atmospheric signatures exist across all observed spectra. To characterize these spectral artifacts, we averaged the spectra together at locations within our map that contain little to no astronomical Hα emission above our sensitivity limit. We then subtract this average off-target spectrum from our observed spectra to effectively remove these signatures. To ensure that the off-target spectra accurately characterized the sky for that region of the map, this procedure was repeated for four Galactic latitudinal subregions. We display stacked spectral image with before (top panel) and after (bottom panel) samples of this reduction process for a subset of our observations in Figure 2.

Overall, the vertical atmospheric features at $v_{\rm GEO} \approx +150$, $+180$, and $+230\ {\rm km\ s^{-1}}$ have been greatly reduced. However, some of this residual atmospheric emission remains, especially at $v_{\rm GEO} \approx +180\ {\rm km\ s^{-1}}$ for spectrum channels > 350 that correspond to a region on the sky between $(l,\ b) = (265°,\ -20°)$ and $(285°,\ -25°)$. These atmospheric residuals persist in these spectra because the Galactic latitude region had few good Hα faint off locations. Although the presence of this lingering atmospheric emission in our final reduced Hα emission map is not ideal, it does not impact the final results of this paper as we do not use the data in that region of the sky in our mass calculation.

3.4. Observational Cutoffs and Degradation Correction

We removed sightlines that are within a 0.55° angular radius of stars that are $m_{\rm V} \leqslant 6.0$ mag as their stellar continuum contributes nonlinear emission to the Hα spectra. This cutoff removes 689 observations from our sample, corresponding to roughly 12% of our observations. Because WHAM is a remote observatory configured for queue observing and does not

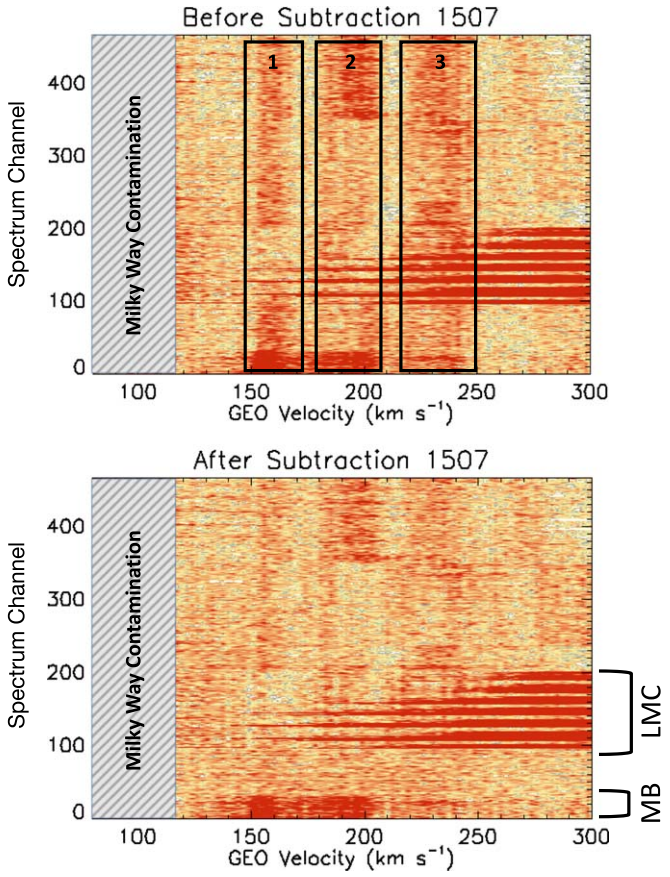

Figure 2. (Top panel) A latitude subregion between $-45 \leqslant b \leqslant -36$ containing 466 WHAM spectra before the removal of residual signatures. At various locations of $v_{\rm GEO} = +155$, $+195$, and $+230$ km s^{-1}, vertical structures are visible within the blue-dashed rectangles, labeled 1, 2, and 3. (Bottom panel) After the correction there is a large improvement in the removal of the vertical signatures. At those same velocities as the top panel, the signatures are reduced. In both panels, emission from the LMC is visible as horizontal stripes over channels 100–200, while the MB is visible from channels 0–35 at lower velocities.

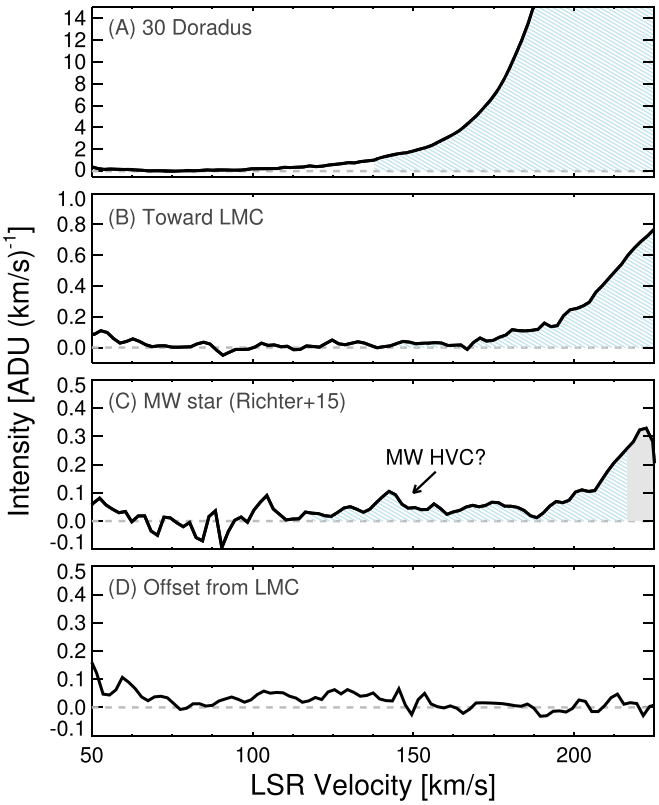

Figure 3. Four examples of Hα spectra that probe different positions in our survey. These include emissions toward: (Panel (A)) 30 Doradus at $(l,\ b) = (279.5°, -31.7°)$, (Panel (B)) the LMC's disk at (278.3°, −31.0°), (Panel (C)) the MW star used in the Richter et al. (2015) study (279.9°, −37.1°), and (Panel (D)) off the LMC's disk at (271.7°, −29.7°). In these panels, we shade material that coincides with the H I disk of the LMC in light gray (only Panel (C) over the displayed LSR velocities) and LMC IVC material out to a line-of-sight velocity of $|v_{\rm LOS}| = 100$ km s^{-1} of its disk in light blue.

require constant monitoring during good weather conditions, we double checked all of the observations that were taken at the optimal charge-coupled device (CCD) temperature for the WHAM camera of $T_{\rm CCD} = -101.2$ °C and not during an automated liquid nitrogen fill to reduce noise. We confirmed that the etalon pressures were stable and that the monitored values matched the input values during the set up of the observations at night. We also ensured that all of the used observations were taken when the outside humidity was less than 85%, at a zenith distance less than 75°, and during dark time observations. Throughout this process a total of 291 additional observations (or around 4%) of the remaining sample were removed. In total, there were 980 observations (or 14%) removed from our sample leaving 5931 observations. For sightlines with repeat observations, we averaged the spectra together. Our survey samples a total of 1712 unique sightlines, where each sightline was observed an average of 3.5 times with the locations toward the LMC's H I disk sampled the most. Figure 3 shows various spectra contained in our survey.

As a result of WHAM instrument degradation over time, observations suffered up to a 20% decrease in observed Hα intensity (Smart et al. 2019). The procedure used for determining the WHAM instrument degradation trend with time is outlined in Haffner et al. (2003). However, our intensity correction does not include a night-to-night intensity calibration associated with air-mass variations that are due to variations in atmospheric conditions. This is because there were insufficient calibration observations taken each night during this survey, in part because there are few WHAM calibration targets in the southern sky.

3.5. Extinction Correction

Previous absorption-line spectroscopic studies toward LMC stars (e.g., Howk et al. 2002; Lehner & Howk 2007; Lehner et al. 2009; Barger et al. 2017) indicate that the gas clouds surveyed in this study exist between us and the LMC. Additionally, Barger et al. (2017) found compelling evidence that the gas within $\Delta v_{\rm LOS} \approx 100$ km s^{-1} from the H I disk of the LMC along the line of sight is associated with large-scale galactic outflow. Similarly, the depletion patterns observed by Lehner et al. (2009) for the HVC material that is in the same projected region on the sky also indicates that this cloud contains dust. We, therefore, applied two extinction corrections: one for attenuation due to the MW and another for self-extinction of the gas clouds assuming that they have a chemical composition similar to that of the LMC.

To correct for reddening, we used the following relationship from Diplas & Savage (1994) that relates the color excess with

the average $N_{\rm H\,I}$ foreground emission:

$$E(B-V)=\frac{\langle N_{\rm H\,I}\rangle}{4.93\times10^{21}\,{\rm atoms/(cm^2\,mag)}}. \quad (1)$$

We used the LAB Galactic H I survey (Hartmann & Burton 1997; Kalberla et al. 2005) to calculate the average foreground H I emission. For the MW, we integrated the H I emission over the $-100\leqslant v_{\rm LSR}\leqslant+100\,{\rm km\,s^{-1}}$ velocity range and assumed an extinction parameter of $R_{\rm v}=3.1$. Similar to the Barger et al. (2013) study, we also adopt the Cardelli et al. (1989) optical extinction curve. Combined, the total extinction for the MW dust is then given by

$$A({\rm H}\alpha)=5.14\times10^{-22}\langle {\rm N_{H\,I}}\rangle\,{\rm cm^{-2}\,atoms^{-1}\,mag}, \quad (2)$$

where the extinction corrected intensity is then $I_{\rm H\alpha,corr}=I_{\rm H\alpha,obs}e^{A({\rm H}\,\alpha)}$. After correcting for extinction associated with foreground MW material, our observed Hα intensities increase by roughly 10%.

The self-extinction by the CGM is small as this gas is diffuse. Following a similar process to the MW extinction, we can account for the self-extinction of the winds by adopting the extinction parameter for the LMC measured by Gordon et al. (2003) of $R_{\rm v}=3.41$. We used an $R_{\rm v}$ that is measured for the LMC's disk as the IVC and HVC material likely originated from this galaxy via stellar feedback events. When we integrated the H I emission across the velocity range of our wind, $+100\leqslant v_{\rm LSR}\leqslant+225\,{\rm km\,s^{-1}}$, we found that the associated self-extinction correction is much less than 1%, and therefore, we neglected this correction in our mass calculations below.

4. Large Magellanic Cloud Standard of Rest (LMCSR) Velocity Frame

When exploring the circumgalactic material of the LMC, it is useful to use a reference frame centered around the LMC disk rather than the LSR frame. We refer to this reference frame as the LMCSR frame. Because the LMC is actively forming stars across its H I disk, the kinematic width of its disk varies rapidly at small scales. Across a slice through the LMC's disk at the Galactic latitude of $b=-31.67°$ and centered on the 30 Doradus starburst region, the width varies from $25\lesssim\Delta v_{\rm H\,I}\lesssim50\,{\rm km\,s^{-1}}$ (see Figure 4). This multiple component structure complicates the process of determining where the disk kinematically ends and where a wind begins.

Across the roughly 10° Galactic longitude slice shown in Figure 4, the motion of the H I gas has a velocity gradient that spans from $+225\lesssim v_{\rm LSR}\lesssim+275\,{\rm km\,s^{-1}}$ at higher Galactic longitudes of $l\approx282°$ to $+275\lesssim v_{\rm LSR}\lesssim+325\,{\rm km\,s^{-1}}$ at $l\approx276°$. Along this velocity slice, there are several locations containing holes where little to no H I exists. This is not surprising as these holes can be created by energetic stellar feedback process activity occurring inside the disk, which heats and ionizes the surrounding gas. This feedback can further drive circumstellar and interstellar material outward, possibly contributing to a galactic outflow as noted by Staveley-Smith et al. (2003). In the LMCSR velocity frame, the spatially varying velocity gradient in the LSR frame is removed, which helped us disentangle the disk and the wind material.

To convert our spectroscopic observations from the LSR to LMCSR velocity reference frame, we initially used the relationship provided by Lehner et al. (2009), which described the motion of the LMC's disk stars. However, galaxy interactions have disrupted the LMC's disk so that the gaseous and stellar components do not align. While the Lehner et al. (2009) LSR to LMCSR relationship works reasonably well for the motion of the gas toward the disk, our observations extend $\Delta\theta\gtrsim5°$ off the LMC's gaseous disk on all sides and is no longer centered in that velocity reference frame. Instead, we modeled the H I emission the LMC and its surroundings to convert our Hα observations into an LMCSR velocity reference frame. This is especially beneficial because the gaseous H I emission extends much further than the stellar disk and because Hα emission tends to kinematically follow the H I emission in HVCs (e.g., Haffner et al. 2001; Putman et al. 2003; Hill et al. 2009; Barger et al. 2012, 2013, 2017; Antwi-Danso et al. 2020).

We determined the motion of the LMC's H I disk by performing a Gaussian decomposition of H I GASS spectra across our surveyed region. We enforce that the Gaussian fits meet the following criteria: each fit must have a column density above $\log(N_{\rm H\,I}/\,{\rm cm^{-2}})\approx19$, kinematic width of approximately $30\,{\rm km\,s^{-1}}$, and a velocity centroid between $+175\leqslant v_{\rm LSR}\leqslant+325\,{\rm km\,s^{-1}}$ to be considered part of the LMC disk. We modeled the H I disk as a simple 2D plane using a least-squares fit. To improve the accuracy of this plane, we weighted our fit by

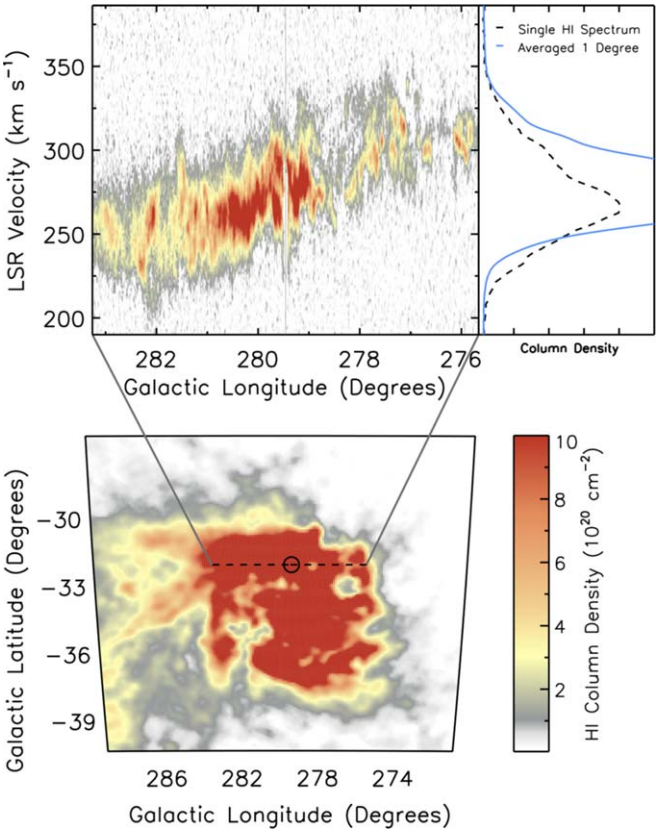

Figure 4. (Bottom panel) An H I intensity-weighted position-position map of the LMC. The circle marks the location of 30 Doradus at $(l,\ b)=(279.46°,\ -31.67°)$ and the dashed line indicates the extent of the Galactic longitude range considered in the top-left panel. (Top-left panel) A position–velocity map of H I emission running through the location of 30 Doradus. (Top-right panel) H I spectra toward the 30 Doradus sightline. The dashed line represents a single ATCA H I spectrum toward 30 Doradus, while the solid blue curve depicts an average spectrum for all emission within circular area of 1° diameter centered on 30 Doradus.

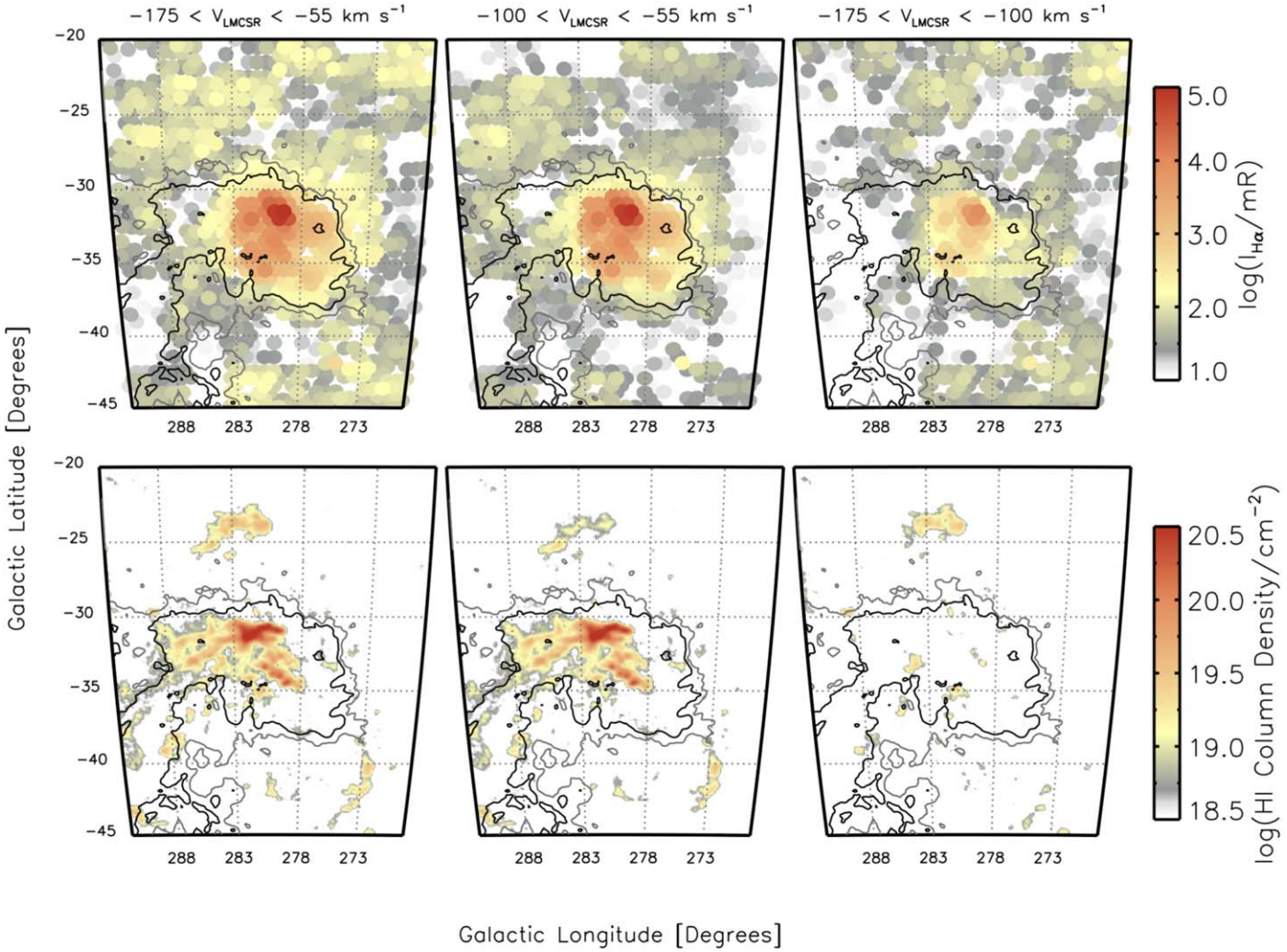

Figure 5. (Top) Hα emission maps of the LMC and its surroundings. This map traces the material that is blueshifted relative to the LMC. From left to right, the total wind integrated over the $-175 \leqslant v_{\rm LMCSR} \leqslant -55$ km s^{-1} velocity range, the IVC portion integrated over the $-100 \leqslant v_{\rm LMCSR} \leqslant -55$ km s^{-1} velocity range, and the HVC portion integrated over the $-175 \leqslant v_{\rm LMCSR} \leqslant -100$ km s^{-1} velocity range. The overlaid black contours trace the H I emission across the same integration range at $\log(N_{\rm H\,I}/{\rm cm}^{-2}) = 19$. (Bottom) H I column density map covering the same region and velocity ranges above using GASS data.

the H I column density. Our resultant relationship between the line-of-sight Galactic longitude (l) and latitude (b) and the central velocity offset is

$$\frac{\Delta v_{\rm LMCSR}}{\rm km\ s^{-1}} = 262.55 - 3.25(l - 280) + 3.66(b - 33). \quad (3)$$

This offset corresponds to an LMCSR velocity as follows: $v_{\rm LMCSR} = v_{\rm LSR} + \Delta v_{\rm LMCSR}$. We used the width of the H I lines out to 3 standard deviations to describe the thickness of the LMC's H I disk and to distinguish between disk and wind material. The nearside and farside disk boundaries are described by the difference between the 3 standard deviation fitted plane and the central velocity (Equation (3)). This results in adopting an LMC disk width of roughly 80 km s^{-1} across the face of the LMC, or 40 km s^{-1} from the kinematic center of the disk to its edge. The newly constructed velocity frame improves our ability to separate the wind material from the LMC's disk that lies in front of the galaxy and to identify the wind material that extends past its H I disk.

5. Kinematic Morphology of Hα Emission

We observe blueshifted material at the intermediate and high velocities relative to the LMC in both H I and Hα emission. This emission is consistent with the results of previous UV absorption-line spectroscopy studies that suggest a large-scale galactic wind emanating from the LMC, driven by the stellar activity within its disk (Howk et al. 2002; Lehner & Howk 2007; Barger et al. 2016). The H I IVC emission is strong toward the LMC's disk and rapidly decreases radially. The Hα emission similarly decreases radially away from the LMC yet extends off the boundary of the LMC stellar ($r_\star \sim 2.15$ kpc) and H I disk at $\log({\rm H\,I}/\ {\rm cm}^{-2}) \approx 19$ (see the left-hand panel of Figure 5). This Hα emission is asymmetric, relative to the H I, such that it extends farther along the edge of the LMC disk near the 30 Doradus starburst region.

Gaseous debris has littered the surrounding area of the LMC due to its interactions with the SMC. Therefore, in addition to the wind that is likely associated with the LMC, there is Magellanic tidal material and MW HVCs that pollute this region of the sky. At higher Galactic latitudes than the LMC ($b \geqslant -27°$), there are a few sparse H I clouds that are likely

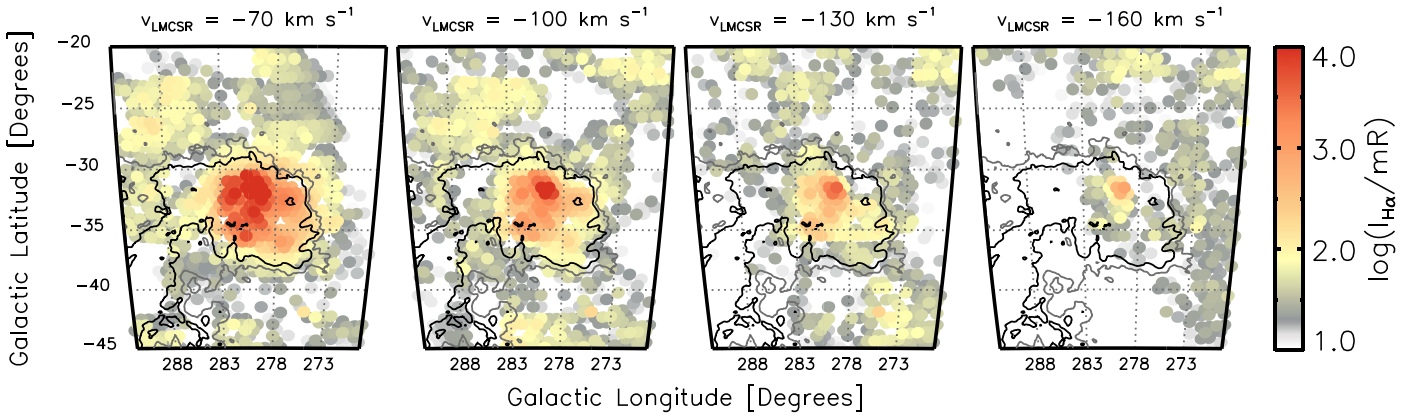

Figure 6. Hα emission channel maps centered at $v_{\rm LMCSR} = -70$, -100, -130, and -160 km s^{-1} (left to right). Widths of these velocity slices are all $\Delta v = 30$ km s^{-1}. The bright emission in the right-hand panel at $\log(I_{\rm H\alpha}/{\rm mR}) \approx 2.5$ spatially aligns with the 30 Doradus starburst at $(l,\ b) = (279.5°,\ -31.7°)$. H I column density contours are drawn at $\log(N_{\rm H\,I}/{\rm cm}^{-2}) = 19.0$ and 20.0 in gray and black, respectively.

associated with the Leading Arm (LA) complex LA I near $(l,\ b) \approx (283°,\ -24°)$; for more details on the Hα distribution of these offset clouds, see B. M. Smart et al. (2021, in preparation). Likewise, because the MB connects the LMC and SMC, its emission is present at $l \geqslant 285°$ with similar velocities as the high Galactic longitude edge of the LMC. Toward the southern rim of the LMC disk, there are fragmented clouds centered on $(l,\ b) = (273°,\ -41°)$, $(278°,\ -38°)$ and $(281°,\ -42°)$ (see the right-hand panel of Figure 5). The background halo star that Richter et al. (2015) used to establish the distance of an HVC ($d_\odot \leqslant 13.3$ kpc) at the location $(l,\ b) = (279.9°,\ -37.1°)$ lies within the region of these low-latitude fragmented clouds. These clouds overlap in velocity with the HVC absorption ($v_{\rm LMCSR} \approx -150$ km s^{-1}) along this stellar sightline, suggesting that it could be associated with the MW. For this reason, we conservatively do not consider gas that is more than a few degrees off of the LMC's H I disk to be part of the LMC outflow.

We find the gaseous material toward the LMC that is the least blueshifted (i.e., kinematically closest to the LMC's motion) morphologically follows the H I disk of the LMC. In Figure 6, we separate the Hα into four separate emission maps, each with small integration ranges that allow us to study the bulk properties of the gas cloud in discrete slices of velocity. The emission at $v_{\rm LMCSR} \approx -100$ km s^{-1} maintains an intensity well over $I_{\rm H\alpha} \approx 0.3$ R across the face of the LMC (see the left two panels of Figure 6). This widespread Hα emission of the IVC is consistent with a large-scale LMC outflow.

At higher velocities, approaching the more blueshifted material, our data shows the emission has a strong spatial alignment with the most active star-forming region within the LMC, 30 Doradus (see the right two panels of Figure 6). This emission spans over $\Delta v_{\rm LOS} \gtrsim 150$ km s^{-1} and remains stable across each channel map toward the star-forming region. Detecting strong Hα emission out to velocities of nearly $\Delta v_{\rm LMCSR} \approx -150$ km s^{-1} while also observing a connection to the lower velocities in the same region indicates an association with the LMC.

6. Intermediate-velocity Gas

We find numerous clouds that are bright in Hα emission that are blueshifted by roughly 50–100 km s^{-1} relative to the LMC's H I disk (Figures 5 and 6). Most of this intermediate-velocity material spatially aligns with the disk of the LMC, resembling a galactic outflow previously suggested (Howk et al. 2002; Barger et al. 2016). Using emission across 1712 Hα sightlines toward the LMC IVC, we determine its mass, its mass-flow rate, and mass-loading factor. In the following LMC IVC mass calculations, we only include the material that is within $\Delta\theta \approx 1°$ of the LMC H I disk with $\log({\rm H\,I}/\,{\rm cm}^{-2}) \gtrsim 19$. This is because some of the Hα emission that is projected multiple degrees off its disk could be associated with Magellanic tidal debris (i.e., MB, Leading Arm) or MW HVCs (see Figure 5 and Section 5).

6.1. Mass Estimate of IVC

Barger et al. (2016) estimated the mass of the intermediate-velocity outflowing LMC winds to be $\log(M_{\rm ionized}/M_\odot) \gtrsim 7.16$ for the low-ionization species. Because they found that this wind is roughly symmetrical on either side of the LMC's disk, this would correspond to a mass of $\log(M_{\rm ionized}/M_\odot) \gtrsim 6.86$ for only the nearside ionized outflow. However, as that study only sampled the wind along two neighboring sightlines via absorption-line spectroscopy, they had to make assumptions about the spatial extent and morphology of the wind. With our kinematically resolved, nearside Hα emission map of the wind of the LMC, we are able to measure both of these directly.

In contrast with the absorption-line work, our Hα survey allows us to obtain a mass estimate more naturally from the wind's density times its volume, $M = \rho {\rm V}$. We calculate its mass density using the electron number density as a proxy for the density of protons as they are roughly equal (i.e., $n_p \approx n_e$) and use a reduced mass of $\mu \approx 1.4 m_{\rm H}$ to account for the contribution from helium and metals. Calculating the volume of the wind requires knowing its solid angle Ω, line-of-sight depth L, three-dimensional geometry (see Figure 8), and distance D. We also include a $\cos(i)$ factor to account for the inclination of the cross-sectional area of the wind relative to our line of sight. The mass is then given as: $M = \mu n_e \Omega D^2 L \cos(i)$. For gas at the distance of the LMC, the mass enclosed within one WHAM beam with $\Omega = 1°$ is then:

$$\frac{M_{\rm ionized}}{M_\odot} = 2.1 \times 10^4 \cos(i) \left(\frac{D}{50\ {\rm kpc}}\right)^2 \left(\frac{L_{\rm H^+}}{\rm pc}\right) \left(\frac{n_e}{\rm cm^{-3}}\right). \quad (4)$$

We estimate the total mass of the wind by summing the single beam mass across the projected outflow area. For the 1712 Hα spectra that fill our map of the LMC (Figure 5), we define the

Table 1
Observed Velocities and Emission Measures

Outflow Component	$v_{\rm LMCSR}$ (km s^{-1})	$\langle {\rm EM} \rangle$[a] (10^{-3} pc cm^{-6})
IVC	−100 to −55	390
HVC	−175 to −100	205

Note.
[a] This is an average emission measure across the corresponding velocity range used to calculate the ionized mass across all sightlines considered to be part of the wind.

morphological extent of the LMC's galactic wind to include regions that are within 1° of its H I disk with neutral column densities larger than $\log(N_{\rm H\,I}/\,{\rm cm}^{-2}) \geqslant 19.0$. This region contains 215 WHAM sightlines contained within roughly 50 deg^2 that are used for our mass estimate. For each of these sightlines, we integrated across the $-100 \leqslant v_{\rm LMCSR} \leqslant -55$ km s^{-1} velocity range to measure the Hα intensity of this wind and to explore its spatial distribution (see Equation (3)). The strength of the Hα recombination line is directly proportional to the electron density squared along the line-of-sight depth and the electron temperature (T_e) of the gas as

$$\frac{I_{\rm H\alpha}}{\rm R} = 0.364\, T_4^{-0.924}\left(\frac{\rm EM}{\rm pc\ cm^{-6}}\right), \quad (5)$$

where EM is the emission measure (EM $\equiv \int n_e(s)^2 ds$) and T_4 is given in units of 10,000 Kelvin (i. e.,$T_4 = T_e/10^4$ K). Measurements of the average EM and associated velocity range are given in Table 1.

Since we cannot measure the line-of-sight depth or the electron density as a function of depth directly, we adopt a few necessary assumptions to estimate the mass of the wind that closely follow the procedures used in prior WHAM Hα studies for evaluating the mass of HVCs (e.g., Hill et al. 2009; Barger et al. 2012, 2017; Smart et al. 2019).

6.1.1. Line-of-sight Depth

The most difficult of these assumptions pertains to the depth and line-of-sight distribution of the wind. Past studies of the HVC component of the LMC wind observed similar kinematics for the neutral and low-ionization species (e.g., Lehner et al. 2009). Moreover, observations of both Hα and H I in outflows of other galaxies (e.g., M82; Lehnert et al. 1999 and Schwartz & Martin 2004) support a multiphase wind that is well mixed at large scales. In our study, due to our large angular resolution at 1°, we are spatially resolving the wind at the kiloparsec scale and are unable to resolve small-scale structure in the wind. We therefore assume that the neutral gas and ionized gas are well mixed at the scales we are probing in our survey such that the ionized hydrogen depth is roughly equal to the neutral depth, i.e., $L_{\rm H^+} \approx L_{\rm H\,I}$.

To estimate this depth, we analyze the fiducial simulations of Bustard et al. (2020) for LMC-specific outflows (see Figure 7). These magnetohydrodynamic simulations used the observed LMC star formation history from Harris & Zaritsky (2009) to the seed star cluster particles that would subsequently deposit the thermal, kinetic, and cosmic-ray energy into surrounding grid cells. In these simulations, gas that emerged from the

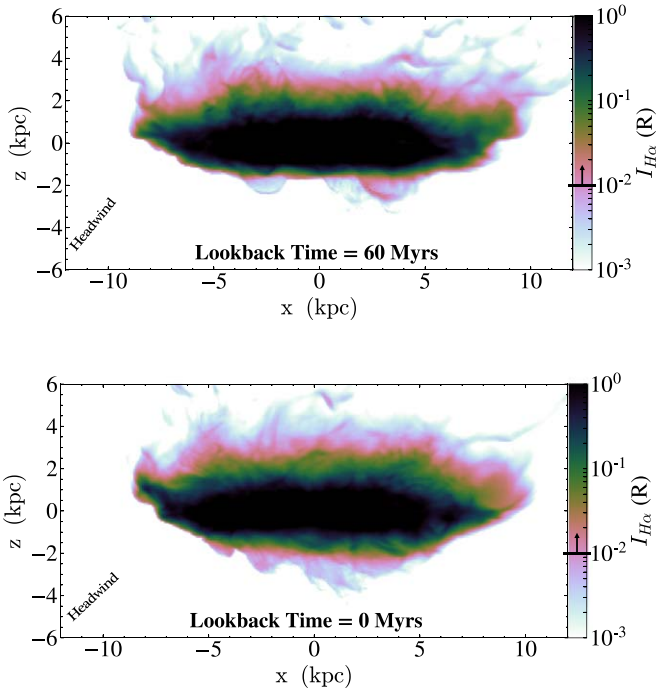

Figure 7. Simulated Hα emission maps from Bustard et al. (2020) of the LMC's galactic wind from an edge-on perspective, using the Trident package (Hummels et al. 2017). This wind is assumed to be in photoionization equilibrium with the UV background (no local ionizing sources from the LMC or MW are included). This model uses the orbital history of the LMC from the models of Besla et al. (2012), the present-day infall velocity of the LMC is 258 km s^{-1} directed edge-on, and 194 km s^{-1} directed face-on with respect to the LMC; the ambient medium is assumed to be smooth with a total gas number density of $\sim 10^{-4}$ cm^{-3} at the present-day LMC distance of $d_\odot \approx 50$ kpc (Salem et al. 2015). (Top) Hα emission at a lookback time of 60 Myr. (Bottom) Current day edge-on view of the LMC and its Hα emission. The arrow in the lower-left corner of each panel represents the motions of the headwind caused by the LMC's path through the MW halo. On each colorbar, the sensitivity of our observations (10 mR) is marked with a horizontal line and an arrow pointed upward.

LMC's disk due to stellar driven outflows experienced an external pressure by surrounding coronal gas. Bustard et al. (2020) found that the apparent coronal gas wind pushes against the leading edge of the LMC via ram pressure and that its effects are strong enough to suppress the nearside outflows and alter the shape of the LMCs halo. While this simulation neglects the gravitational influence of the SMC and MW, we expect the depth of the outflow to be primarily influenced by the LMCs gravitational potential and ram-pressure effects.

On a global scale, the galactic winds produced in the Bustard et al. (2020) simulations match well kinematically and spatially with the observed LMC outflow. We use the Bustard et al. (2020) results as a guide for constraining the depth of this wind. They find that the 10^4 K gas in the nearside outflow penetrated to a height of $z_{\rm wind} \approx 3$ kpc below the midplane of the LMC ($z_{\rm midplane} = 0$ kpc) at a lookback time of 60 Myr. At present-day, they find that this wind stalls at a height of $z_{\rm wind} \approx 4$ kpc due to ram pressure. The outflows on the farside of the LMC, however, are able to travel much further off the disk as ram-pressure effects are weaker on the trailing side of the galaxy. Accounting for the height of the LMC's H I disk ($z_{\rm H\,I,disk} \approx 1.75$ kpc), this corresponds to a present-day wind depth of roughly $1 \leqslant L_{\rm wind} \leqslant 2$ kpc off the galaxy.

We used this depth to calculate an average electron density for the LMC's galactic wind using the measured EM as

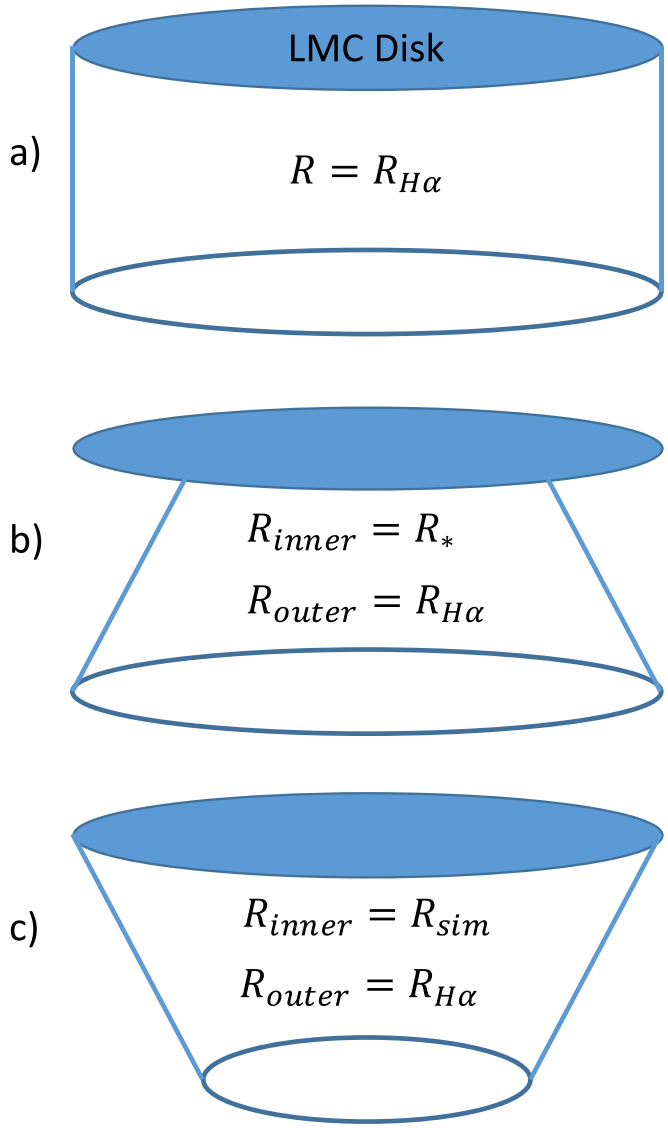

Figure 8. Explored nearside volume geometries of the LMC outflow, including (a) a cylinder with a uniform outflow that spans the face of the galaxy out to some height, (b) a partial cone with its narrow end embedded and centered on a region of intense star formation, and (c) an inverted partial cone with its narrow side pointing away from the LMC's disk to match the morphology of the simulated galactic outflow under influence of ram pressure and headwinds.

$\langle n_e \rangle = \langle \mathrm{EM} \rangle^{1/2} L_{\mathrm{H}^+}^{-1/2}$. We then used this density to calculate the outflow's mass with Equation (4). Although our main uncertainty involves the depth of the wind, it is important to note that the mass scales as $M_{\mathrm{ionized}} \propto L_{\mathrm{H}^+}^{-1/2}$, resulting in only a modest variance in mass when we consider a range of reasonable depths. Moreover, we assume an electron temperature in the range of $0.8 \lesssim T_4 \lesssim 1.2$, which is where the H$\alpha$ emission peaks. We further assume that the temperature of the neutral and ionized hydrogen gas are roughly equal allowing us to relate the neutral and ionized hydrogen number densities for a given pressure scenario as $P_{\mathrm{ionized}}/n_{\mathrm{ionized}} = P_{\mathrm{neutral}}/n_{\mathrm{neutral}}$ under ideal gas conditions.

Because the LMC is nearly face-on, we cannot constrain how the morphology of the wind varies with depth as we only see its two-dimensional projection on the sky. Therefore, we acknowledge three separate volume scenarios: cylinder, partial outward flaring cone, and partial tapered cone (see Figure 8). For the cylindrical wind in scenario (a), we simply assume that the radius of the wind is constant and matches the extent of the Hα emission. We include the outward flaring partial cone geometry in scenario (b) as it has been observed for other galaxies (e.g., M82); in this scenario, we set the inner cone radius to the stellar radius (2.15 kpc) and the outer radius to match radius of the Hα emission. The tapered, inverted cone in scenario (c) is the geometry that resulted for the nearside LMC wind from Bustard et al. (2020) simulation when they accounted for ram-pressure effects; in this scenario, we match the radii to match the simulation and the Hα observations. For these three geometries, the nearside wind masses would correspond to $\log(M_{\mathrm{ion}}/M_\odot) = 7.36 \pm 0.14$ for volume (a), $\log(M_{\mathrm{ion}}/M_\odot) = 7.10 \pm 0.14$ for volume (b), and a mass of $\log(M_{\mathrm{ion}}/M_\odot) \leqslant 7.09 \pm 0.14$ for volume (c). As we cannot observationally determine which of these wind geometries better matches with the LMC's nearside galactic wind, we report the values of the cylindrical scenario in the text as it is the simplest volume that requires the least assumptions. We report the values and ranges for the other two volume scenarios in Table 2. To estimate the total mass of the neutral and ionized gas of this wind, we assume the outflow is symmetric on both the nearside and farside of the LMC's disk and that it has an ionization fraction of $n_{\mathrm{H}^+}/n_{\mathrm{H}} \approx 0.75$ (Barger et al. 2016). We found the total IVC mass of the wind to be in the range of $7.70 \leqslant \log(M_{\mathrm{total}}/M_\odot) \leqslant 7.85$. This is compared to the previous Barger et al. (2016) estimate of $\log(M_{\mathrm{ionized}}/M_\odot) \gtrsim 7.16$.

We calculate the mass-flow rate for this wind by assuming an outflow time of ($t_{\mathrm{outflow}} \approx 60$ Myr). This is calculated using information regarding the last period of star formation ($\sim$100 Myr) as well as the time necessary for the wind to penetrate through the surrounding medium and travel approximately 2 kpc off the H I disk. This results in a total IVC mass-flow rate of $0.83 \leqslant \dot{M}_{\mathrm{outflow}} \leqslant 1.18\ M_\odot\ \mathrm{yr}^{-1}$. The mass-loading factor is also calculated to study the ratio of the mass-flow rate to the star formation rate, ($\eta \equiv \dot{M}_{\mathrm{outflow}}/\dot{M}_\star$). We adopt a star formation rate in the range of $0.3 \lesssim \dot{M}_\star \lesssim 0.34\ M_\odot\ \mathrm{yr}^{-1}$ to agree with the star formation history of the LMC (see Figure 11 of Harris & Zaritsky 2009). This results in a mass-loading factor between $2.44 \leqslant \eta \leqslant 3.93$. Because the mass-loading factor, ($\eta \equiv \dot{M}_{\mathrm{outflow}}/\dot{M}_\star$), is much greater than unity, this indicates that the current star formation state of the LMC is unsustainable such that the galaxy could become quenched if this state is prolonged and if the ejected gas is able to escape.

Table 2
Mass Estimates for the IVC and HVC Material of the LMC Outflow

Outflow Geometry	M_{ion} ($M_\odot$)	M_{total} ($M_\odot$)	$\dot{M}_{\mathrm{outflow}}$ ($M_\odot\ \mathrm{yr}^{-1}$)	η
IVC				
Cylinder	7.28–7.43	7.70–7.85	0.83–1.18	2.44–3.93
Outward cone	7.02–7.17	7.44–7.59	0.46–0.65	1.35-2.16
Inward cone	7.01–7.16	7.43–7.58	0.45–0.63	1.32–2.11
HVC				
Cylinder	6.93–7.05	7.35–7.47	0.37–0.49	1.09–1.63

Note. All values for M_{total} assume a symmetrical wind on the nearside and farside of the LMC with an ionization fraction of $n_{\mathrm{H\ II}}/n_{\mathrm{H}} = 0.75$ that includes neutral and ionized gas assuming a reduced mass of $\mu \approx 1.4 m_{\mathrm{H}}$ to account for helium and metals. We used the values listed in Table 1 to calculate these outflow masses and rates.

6.2. Discussion of IVC Material

Barger et al. (2016) characterized the IVC material with respect to the LMC using UV absorption-line spectroscopy toward an LMC disk star and a background QSO. They found the nearside material to have an estimated mass of $\log(M_{\rm low\ ions}/M_\odot) \gtrsim 7.16$ for low-ionization species on both the nearside and farside of the galaxy. This corresponds to an ionized mass of $\log(M_{\rm ionized}/M_\odot) \gtrsim 6.9$ for gas traveling up to $\Delta v_{\rm LMCSR} \approx -100\ {\rm km\ s^{-1}}$ on the nearside of the LMC. Over the same velocity range, we calculated the ionized hydrogen mass to be $\log(M_{\rm ionized}/M_\odot) \approx 7.36$ (see Section 6). While our estimate is larger than the Barger et al. (2016) nearside mass, it is important to note the discrepancies between our estimates can be attributed to how each study determined the masses.

In the Barger et al. (2016) study, they assumed (1) the wind has an angular extent similar to the LMC's H I disk ($R_{\rm H\,I} \approx 3.7$ kpc), (2) a covering fraction of $f_\Omega = 0.7$ for low-ionization and $f_\Omega = 0.9$ for high-ionization species, and (3) the average global strength for this wind could be represented by the absorption they observed along their two sightlines. We, however, find that the Hα emission of the wind extends around 1° on average off the H I disk, which means that the outflow radius is roughly 1 kpc larger (i.e., $R_{\rm H\alpha} \approx R_{\rm H\,I} + 1$ kpc). Their third assumption may result in a significantly underestimated outflow mass as the two sightlines used in the Barger et al. (2016) study probed a relatively quiescent region of the LMC. We emphasized the effect of their assumptions by taking the average emission measure from the same region as the Barger et al. (2016) sightline—in the opposite quadrant as 30 Doradus—and calculating a corresponding mass for an area similar to theirs. Using $\langle {\rm EM} \rangle \approx 0.2$ pc cm^{-6}, the outflow mass would be $\log(M_{\rm ionized}/M_\odot) \approx 7.1$, which is nearly half as large as our IVC cylindrical mass estimate and nearly in agreement with the Barger et al. (2016) estimate for the low-ionization species.

Ultimately, the fate of this ejected material remains uncertain. The escape velocity of the LMC is roughly 110 km s^{-1} (Besla 2015), which corresponds to roughly 100 km s^{-1} along the line of sight for an inclination of around 25°. Therefore, the majority of the IVC material is not expected to escape. However, the Magellanic System is a crowded environment and tidal interactions between the SMC, and possibly the MW, can assist in the removal of otherwise bound gas (see D'Onghia & Fox 2016 for a review). Some of the material from previous outflow events may have been displaced into the trailing Magellanic Stream. In a kinematic investigation of the H I 21 cm emission of the Magellanic Stream, Nidever et al. (2008) found that one of its two filaments traces back to the 30 Doradus region of the LMC. Richter et al. (2013) measured the chemical composition of this "30-Doradus" filament and found that it has a metallicity that is consistent with an LMC origin. Fox et al. (2013) explored the chemical composition of the other Magellanic Stream filament and found that it has a lower metallicity that is more consistent with an SMC origin, which kinematically traces back to the Magellanic Bridge (Nidever et al. 2008).

Ram-pressure stripping may also play an important role in removing gas from the Magellanic Clouds. The impact that ram pressure has on the CGM strongly depends on the density of the medium that it is traveling through and on the motion of the gas within its surrounding medium. Based off the work of Salem et al. (2015), Bustard et al. (2020), and others (Heckman et al. 2000; Mastropietro et al. 2005; Fujita et al. 2009), the effects of ram pressure on gas is multifaceted and either can promote or suppress the removal of gas from a galaxy depending on the circumstance. This is because ram pressure can work in direct opposition of galactic winds positioned on the leading side of a galaxy, where the surrounding coronal gas will act as a headwind that pushes against the outflowing back toward the galaxy. Therefore, the outflow on the nearside of the LMC galaxy, which is the side leading the LMC's orbit through the MW's halo, will be suppressed. Meanwhile, the farside could experience an enhanced outflow as ram pressure will push the gas away from the galaxy and it could therefore be more massive. With ram-pressure stripping, the simulated wind in the Bustard et al. (2020) study was able to reach a height of more than 1.7 kpc off the LMC's H I disk and had a total ejected mass in the range of $6.7 \leqslant \log(M_{\rm ejected}/M_\odot) \leqslant 8.4$. While our IVC mass estimate is within this mass range, Bustard et al. (2020) predicts that a significant portion of this material flows off the farside of the LMC's disk (see their Figure 11), which is the trailing side trails as the LMC traverses the MW's halo. Conversely, the Barger et al. (2016) UV absorption-line study found that the nearside and farside outflows were kinematically symmetric along their explored sightlines, though this might not be representative of the outflow's large-scale structure. A study like this one of the farside—in which the winds are mapped—is needed to determine its physical extent and the impact of ram-pressure stripping.

7. HVC Material

We also detected a high-velocity component to the LMC's galactic wind in Hα emission over the $-175 \leqslant v_{\rm LMCSR} \leqslant -100\ {\rm km\ s^{-1}}$ velocity range (see top-right panel of Figure 5). Much of this material is traveling away from the LMC at speeds that exceed its escape velocity and could therefore be permanently lost from the galaxy. Furthermore, tidal forces could assist in carrying this material away. At these high velocities, the Hα emission is especially concentrated in the direction of the 30 Doradus starburst region (refer to the right panel of Figure 6). We calculate the ionized mass of this HVC using the procedures described in Section 6.1.

Using the timescale of the IVC material (60 Myr) as well as the observed velocities, we estimate the HVC reaches a height up to 9 kpc off the H I disk. It is possible the material reaches even further as Bustard et al. (2020) shows ejected material to reach heights in excess of 13 kpc. With these estimates and Equation (4), we calculate an ionized hydrogen mass of $\log(M_{\rm ionized}/M_\odot) = 6.99 \pm 0.13$ for the HVC. This mass contains 124 WHAM beams that are within roughly 20 deg^2. Following the procedure in Section 6.1, we assume the wind to be symmetrical about the LMC disk and to contain both neutral and ionized material. This corresponds to a total mass of $\log(M_{\rm total}/M_\odot) \approx 7.41$, but we emphasize that this could be a lower limit on its total mass as ram-pressure effects are likely enhancing the farside wind (see Figure 7 and Bustard et al. 2020). Given that this material is the HVC component of the current outflow explored in Section 6.1, the mass-flow rate is $\dot{M}_{\rm outflow} \approx 0.43\ M_\odot\ {\rm yr^{-1}}$ and the mass-loading factor is $\eta \approx 1.36$. The full ranges of these results are provided in Table 2.

When comparing our mass to prior work there is a general agreement. Lehner et al. (2009) estimated its neutral hydrogen gas mass to be $5.7 \leqslant \log(M_{\rm H\,I}/M_\odot) \leqslant 6.0$ with a total mass of at least $\log(M_{\rm total}/M_\odot) > 6.7$ with the assumptions that it has an LMC origin and that it lies at a distance of

$40 \leqslant d_{\odot} \leqslant 50$ kpc away. Using the ionization fraction of $0.5 \lesssim n_{\rm H\,II}/n_{\rm H} \lesssim 0.8$ that Lehner et al. (2009) measured, we calculate a total hydrogen mass (neutral and ionized) in the range of $6.9 \leqslant \log(M_{\rm H}/M_{\odot}) \leqslant 7.1$, which is in agreement with their total mass lower limit. Moreover, simulations from Bustard et al. (2020) estimated $6.56 \leqslant \log(M_{\rm ejected}/M_{\odot}) \leqslant 7.78$ worth of material reaching over 13 kpc away from the LMC disk. If we consider that the bulk of the HVC material distance of the wind to be at $d_{\odot} \approx 13$ kpc, then our observed HVC mass falls within the range of this simulated ejected mass.

7.1. Origins of the HVC

We observe high-velocity material toward the LMC at velocities greater than $100\,{\rm km\,s^{-1}}$ off the LMC H I disk ($+90 \leqslant v_{\rm LSR} \leqslant +175\,{\rm km\,s^{-1}}$), detailed in Section 7. This emission is persistent at intermediate to low velocities relative to the LMC and spatially aligns well with the LMC's H I disk (see Figure 6). These observed properties are consistent with an LMC origin in which the gas is expelled from the galaxy by its stellar activity. This is a conclusion that has also been reached by Staveley-Smith et al. (2003) using an H I emission line and by Lehner et al. (2009) using UV absorption lines (also see Lehner & Howk 2007 and Barger et al. 2016). Staveley-Smith et al. (2003) found that the H I column densities of the HVC peaked at locations that align with H I voids within the LMC disk (such as supergiant shells, e.g., LMC 3); they further identified spatial and kinematic H I bridges that linked back to the LMC's disk. Lehner et al. (2009) used 139 stars embedded in the LMC as background targets in an UV absorption-line study to explore the properties of this HVC; they found that the HVC has (i) an LSR velocity gradient in R.A. that follows the LMC's velocity gradient, (ii) dust based on depletion patterns—signifying a galactic origin (see also Smoker et al. 2015), (iii) an oxygen abundance similar to the LMC of $[{\rm O\,I}/{\rm H\,I}] = -0.51^{+0.12}_{-0.16}$, and (iv) a high covering fraction in the direction of the LMC.

However, since the works mentioned above, the origin of this HVC has been strongly debated. This is because Werner & Rauch (2015) found C II, Si II, and Si III absorption consistent with this HVC in the spectra of a background star at a distance of $d_{\odot} = 9.2^{+4.1}_{-7.2}$ kpc. Richter et al. (2015) confirmed the presence of the HVC in the direction of this star, which places the HVC at a distance of $d_{\odot} < 13.3$ kpc, and asserted that the HVC lies too far from the LMC to be consistent with an LMC origin. They reason that it is unlikely that material ejected from the LMC would be able to reach a distance of roughly 40 kpc intact during the few hundred million years it would take to travel at speeds of $\sim 150\,{\rm km\,s^{-1}}$. This is because, during the cloud's journey it would sustain numerous collisions with not only the CGM of the LMC, but also the halo of the MW. Consequently, Richter et al. (2015) argue that this would strip a large amount of the cloud's material and drag forces would slow the cloud. Needless to say, the time required to make this journey (250–400 Myr; Barger et al. 2016) would consequently lead to a transverse displacement and the cloud would no longer be toward the LMC.

In light of the results presented in this paper, and by previous studies, we offer a mutual theory on the distribution and association of material observed between the MW and LMC. We postulate that there are two HVCs with different origins near the LMC on the sky: (1) an HVC is associated with the galactic winds of the LMC and (2) an HVC that is associated with the MW. Strong evidence for this latter HVC was presented by Werner & Rauch (2015) and Richter et al. (2015), who confirmed that there is high-velocity material at $(l,\ b) = (279.9°,\ -37.1°)$, 3°–5° away from 30 Doradus, that resides at a distance of $d_{\odot} < 13.3$ kpc. This sightline is on the periphery of the Hα emission that spans across the LMC (see Figure 5). Meanwhile, similarities in kinematics, dust depletion, and oxygen abundances strongly indicate that most of the high-velocity material in the direction of the LMC has an LMC origin. Unless the previous evidence gathered from Staveley-Smith et al. (2003), Lehner et al. (2009), and our study is entirely coincidental, there is likely to be more than one complex toward the LMC. Therefore, we argue that the LMC HVC spans a much larger area of the sky in the direction of the LMC and that there is also a smaller HVC positioned just offset from the LMC on the sky, which is associated with the MW.

7.2. Feedback of Low-mass Galaxies

Galactic winds and the ability of a galaxy to retain ejected gas are directly related to the galaxy's capacity to form future stars. These winds tend to intensify as stellar activity increases. Moreover, because lower mass galaxies have smaller gravitational potential wells, their gas is more easily ejected out of them. For massive galaxies, the halo and extraplanar gas that surrounds their disks suppresses outflowing material. This results in a general trend in which the mass-loading factor is diminished for massive galaxies and enhanced in low-mass galaxies. In the case of the LMC, with a stellar mass of $M_{\star} = 3 \times 10^{9}\,M_{\odot}$ (van der Marel et al. 2009) and total mass $M_{\rm total} = 1.7 \times 10^{10}\,M_{\odot}$ (van der Marel & Kallivayalil 2014), as well as an active star formation history (Harris & Zaritsky 2009), it is expected that this galaxy will have a relatively elevated mass-loading factor.

We estimate that the LMC's mass-loading factor ranges from $3.53 \leqslant \eta \leqslant 5.56$ when including both the IVC and HVC gas in its winds and when assuming cylindrical geometry. Our values are relatively large when compared to other studies for galaxies with similar stellar mass (see Figure 9). However, the Barger et al. (2016), Chisholm et al. (2017), and Leethochawalit et al. (2019) studies all used absorption-line spectroscopy, which spatially probes less of the wind; this results in a more uncertain mass estimate as the physical extent of winds are poorly constrained. In the case of the McQuinn et al. (2018) Hα imaging study, although they were able to measure the extent of the wind, their observations were more than a magnitude less sensitive than ours and were unable to detect the diffuse gas in the wind.

The impact of geometry assumptions is most telling when comparing our results with those of the Barger et al. (2016) absorption-line study of the LMC. Although our study shares many of the same assumptions as their study, we were able to map the extent and morphology of the wind, whereas they were forced to make simplistic assumptions for its solid angle. The mass-flow rates from the Barger et al. (2016) and the star formation rates from Harris & Zaritsky (2009) correspond to a mass-loading factor for LMC that is in the range of $0.7 \leqslant \eta \leqslant 0.8$. When we increase their solid angle to match what we observe in Hα emission, their mass-loading factor becomes $1.3 \leqslant \eta \leqslant 1.5$. This revised range is in better agreement with our mass-loading factor for conical geometries (outward and inward cone; see Table 2).

In studies that explore a wide range of galaxy masses, the trend that the mass-loading factor decreases with galaxy mass is

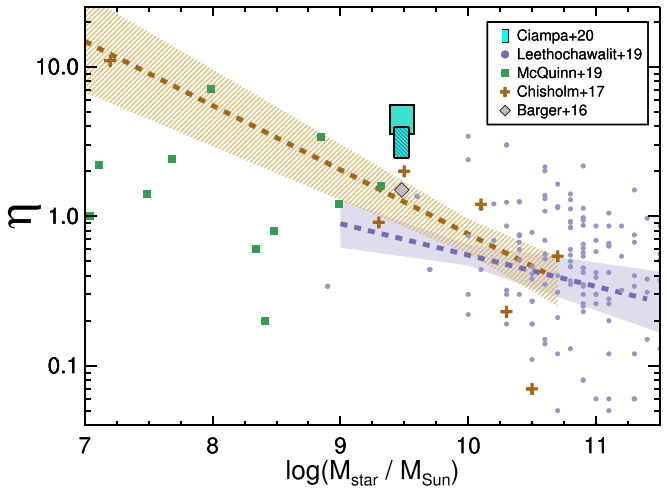

Figure 9. Mass-loading factors from various studies. The mass-loading factor we calculated for the total LMC wind (IVC + HVC) is marked with a cyan bar while solely the IVC component is the darker hashed blue bar. Our results for the LMC wind are found in Table 2. The Barger et al. (2016) LMC loading factor (IVC only) is indicated with a gray diamond after we adjust their outflow mass to match the assumptions used in our study. Green squares mark mass-loading factors from McQuinn et al. (2018), which only include the ionized gas mass in outflows. The brown and purple envelopes are the limits of uncertainty for mass-loading relations from the Chisholm et al. (2017) and Leethochawalit et al. (2019) studies (refer to their Equations (16) and (8), respectively).

clear (see Figure 9). Chisholm et al. (2017) found mass-loading factors ranging from 0.2–19.0 for their sample of eight dwarf star-forming galaxies ($6.9 \leqslant \log(M_\star/M_\odot) \leqslant 10.7$) using UV absorption-line spectroscopy. At the LMC mass, this study predicts a mass-loading factor of around 1.1. Across similar masses, McQuinn et al. (2018) observed their galaxies via Hα imaging and found mass-loading factors ranging from $0.2 \leqslant \eta_{\rm ionized} \leqslant 7.1$ for the ionized gas in the wind only. For more massive galaxies ($9.5 \leqslant \log(M_\star/M_\odot) \leqslant 11.5$), Leethochawalit et al. (2019) found mass-loading factors that range from 0.3–1.0 for their UV absorption-line study. While our largest LMC mass-loading factor estimate is at least twice as large as the Chisholm et al. (2017) and Leethochawalit et al. (2019) trend lines predict, we acknowledge that is in part because of differences in the assumed geometries of the winds. When assuming a conical geometry, a commonly assumed geometry for galactic winds, our mass-loading factor is reduced by nearly 50% and is more consistent with their results (see Table 2).

Still, there is a significant spread in mass-loading factors between studies that requires additional work to reduce. As of right now, no uniform sample exists across low- and high-mass galaxies. Such a consistent sample would go a long way in improving our understanding of the relationship between mass-loading factor and galaxy mass. Further, more imaging or emission-line studies are needed to better constrain the geometry of these winds, though they also need to have a high enough sensitivity to detect the diffuse gas.

8. Summary

We completed the first kinematically resolved survey of the LMC's nearside galactic wind in Hα λ6563 using the WHAM. These mapped observations span $20 \times 20^\circ$ across the sky and comprise 1712 sightlines. By combining these observations with existing H I observations, we were able to determine the extent and morphology of the neutral- and warm-ionized ($T_e \approx 10^4$ K) phases of this wind. Here we summarize the main conclusions of this study:

1. *Morphology and Extent:* We find that diffuse gas in the galactic wind spans across the entire face of the LMC. We additionally find numerous faint $I_{\rm H\alpha} \approx 100$ mR clouds offset from the main wind structure, but we are unable to confidently determine whether or not they are physically associated with the LMC's galactic wind as tidally displaced Magellanic Cloud material and MW HVCs also pollute this region of the sky.
2. *Kinematic Distribution:* We find the bulk of the LMC's galactic wind is moving with velocities of $v_{\rm LMCSR} \lesssim -110\,{\rm km\,s^{-1}}$ relative to the H I disk, which is less than the escape velocity. However, roughly $\log(M_{\rm ion,hvc}/M_\odot) \approx 7.0$, or roughly 44%, of this wind is moving away from the LMC at speeds greater than the escape velocity. Specifically, we find the gas that is spatially aligned with 30 Doradus is moving at the greatest speeds relative to the LMC at $v_{\rm LMCSR} \lesssim -175\,{\rm km\,s^{-1}}$.
3. *Two HVC Complexes toward the LMC:* We find Hα emission at high velocities relative to the LMC that is strongly spatially correlated with 30 Doradus. This emission similarly persists at lower velocities. Our results—in addition to the results from the Staveley-Smith et al. (2003), Lehner & Howk (2007), Lehner et al. (2009), and Barger et al. (2016) studies—lead us to conclude that this starburst region is responsible for generating this HVC (see Figures 3 and 6). The HVC discussed in Richter et al. (2015), which lies a few degrees off the $\log(N_{\rm H\,I}/\,{\rm cm^{-2}}) = 19$ contour of the LMC's H I disk and at a distance of $d_\odot \lesssim 13.3$ kpc, is a different complex. That HVC likely has a MW origin based on their results.
4. *Outflow Mass, Flow Rate, and Loading Factor:* We measure an ionized gas mass in the range of $7.28 \leqslant \log(M_{\rm ionized}/M_\odot) \leqslant 7.43$ for the outflowing material on the nearside of the LMC that is moving at intermediate velocities, i.e., speeds that are within $\sim 100\,{\rm km\,s^{-1}}$ of the LMC's H I disk. The high-velocity component of this wind has an ionized mass of $6.93 \leqslant \log(M_{\rm ionized}/M_\odot) \leqslant 7.05$. Combined, we estimate that the total ionized gas mass in this nearside wind is in the range of $7.44 \leqslant \log(M_{\rm ionized}/M_\odot) \leqslant 7.58$. This corresponds to a total neutral and ionized mass of the entire wind that ranges between $7.87 \leqslant \log(M_{\rm total}/M_\odot) \leqslant 8.0$, assuming that it is symmetrical on the nearside and farside of the LMC and that it is 75% ionized (see Lehner & Howk 2007; Barger et al. 2016). We further calculate a total mass-flow rate and mass-loading factor of $1.20 \leqslant \dot{M}_{\rm outflow} \leqslant 1.67\,M_\odot\,{\rm yr^{-1}}$ and $3.53 \leqslant \eta \leqslant 5.56$. Table 2 summarizes these results.
5. *Undetected Diffuse Material:* We compared our results with existing mass-loading factor trends that vary with stellar mass. We found that our average mass-loading factors are on average roughly 2.5 times larger than both optical Hα imaging and UV absorption-line studies at the stellar mass of the LMC. This indicates that either the observational sensitivity (optical imaging: McQuinn et al. 2018) may be insufficient to detect diffuse gas in these

outflows or that the geometric assumptions are too conservative (UV absorption-line spectroscopy: Barger et al. 2016; Chisholm et al. 2017, and Leethochawalit et al. 2019).

We thank Lister Staveley-Smith and Sungeun Kim for providing us with the ATCA and Parkes telescopes LMC H I survey data cube. This paper includes archived LAB and GASS H I data obtained through the AIfA H I Surveys Data Server (https://www.astro.uni-bonn.de/hisurvey/index.php). WHAM operations for these observations were supported by National Science Foundation (NSF) awards AST-1108911 and AST-1714472/1715623. Madeline Horn received additional support through NSF grant PHY-1358770.

ORCID iDs

Drew A. Ciampa https://orcid.org/0000-0002-1295-988X
Kathleen A. Barger https://orcid.org/0000-0001-5817-0932
Nicolas Lehner https://orcid.org/0000-0001-9158-0829
L. Matthew Haffner https://orcid.org/0000-0002-9947-6396
Brianna Smart https://orcid.org/0000-0002-5012-3549
Chad Bustard https://orcid.org/0000-0002-8366-2143

References

Antwi-Danso, J., Barger, K. A., & Haffner, L. M. 2020, ApJ, 891, 176
Barger, K. A., Haffner, L. M., & Bland-Hawthorn, J. 2013, ApJ, 771, 132
Barger, K. A., Haffner, L. M., Wakker, B. P., et al. 2012, ApJ, 761, 145
Barger, K. A., Lehner, N., & Howk, J. C. 2016, ApJ, 817, 91
Barger, K. A., Madsen, G. J., Fox, A. J., et al. 2017, ApJ, 851, 110
Besla, G. 2015, The Orbits of the Magellanic Clouds, Lessons from the Local Group: A Conference in honour of David Block and Bruce Elmegreen (Cham: Switzerland), 311
Besla, G., Kallivayalil, N., Hernquist, L., et al. 2010, ApJL, 721, L97
Besla, G., Kallivayalil, N., Hernquist, L., et al. 2012, MNRAS, 421, 2109
Bustard, C., Zweibel, E. G., D'Onghia, E., et al. 2020, ApJ, 893, 29
Cardelli, J. A., Clayton, G. C., & Mathis, J. S. 1989, ApJ, 345, 245
Chisholm, J., Tremonti, C. A., Leitherer, C., & Chen, Y. 2017, MNRAS, 469, 4831
Choi, Y., Nidever, D. L., Olsen, K., et al. 2018, ApJ, 866, 90
D'Onghia, E., & Fox, A. J. 2016, ARA&A, 54, 363
de Boer, K. S., & Savage, B. D. 1980, ApJ, 238, 86
de Grijs, R., Wicker, J. E., & Bono, G. 2014, AJ, 147, 122
Diplas, A., & Savage, B. D. 1994, ApJ, 427, 274
Erb, D. K. 2015, Natur, 523, 169
Ford, A. B., Davé, R., Oppenheimer, B. D., et al. 2014, MNRAS, 444, 1260
Fox, A. J., Richter, P., Wakker, B. P., et al. 2013, ApJ, 772, 110
Fujita, A., Martin, C. L., Mac Low, M.-M., New, K. C. B., & Weaver, R. 2009, ApJ, 698, 693
Gordon, K. D., Clayton, G. C., Misselt, K. A., Landolt, A. U., & Wolff, M. J. 2003, ApJ, 594, 279
Haffner, L. M., Reynolds, R. J., & Tufte, S. L. 2001, ApJL, 556, L33
Haffner, L. M., Reynolds, R. J., Tufte, S. L., et al. 2003, ApJS, 149, 405
Harris, J., & Zaritsky, D. 2009, AJ, 138, 1243
Hartmann, D., & Burton, W. B. 1997, Atlas of Galactic Neutral Hydrogen (Cambridge: Cambridge Univ. Press)
Hausen, N. R., Reynolds, R. J., Haffner, L. M., & Tufte, S. L. 2002, ApJ, 565, 1060
Heckman, T. M. 2003, RMxAA, 17, 47
Heckman, T. M., Lehnert, M. D., Strickland, D. K., & Armus, L. 2000, ApJS, 129, 493
Hill, A. S., Haffner, L. M., & Reynolds, R. J. 2009, ApJ, 703, 1832
Howk, J. C., Sembach, K. R., Savage, B. D., et al. 2002, ApJ, 569, 214
Hummels, C. B., Smith, B. D., & Silvia, D. W. 2017, ApJ, 847, 59
Kalberla, P. M. W., Burton, W. B., Hartmann, D., et al. 2005, A&A, 440, 775
Kim, S., Dopita, M. A., Staveley-Smith, L., & Bessell, M. S. 1999, AJ, 118, 2797
Kim, S., Staveley-Smith, L., Dopita, M. A., et al. 1998, ApJ, 503, 674
Kim, S., Staveley-Smith, L., Dopita, M. A., et al. 2003, ApJS, 148, 473
Laval, A., Rosado, M., Boulesteix, J., et al. 1992, A&A, 253, 213
Leethochawalit, N., Kirby, E. N., Ellis, R. S., Moran, S. M., & Treu, T. 2019, ApJ, 885, 100
Lehner, N., & Howk, J. C. 2007, MNRAS, 377, 687
Lehner, N., Staveley-Smith, L., & Howk, J. C. 2009, ApJ, 702, 940
Lehnert, M. D., Heckman, T. M., & Weaver, K. A. 1999, ApJ, 523, 575
Lucchini, S., D'Onghia, E., Fox, A. J., et al. 2020, arXiv:2009.04368
Mastropietro, C., Moore, B., Mayer, L., Wadsley, J., & Stadel, J. 2005, MNRAS, 363, 509
McClure-Griffiths, N. M., Pisano, D. J., Calabretta, M. R., et al. 2009, ApJS, 181, 398
McQuinn, K. B. W., van Zee, L., & Skillman, E. D. 2018, in IAU Symp. 344, Dwarf Galaxies: From the Deep Universe to the Present, ed. K. B. W. McQuinn & S. Stierwalt (Cambridge: Cambridge Univ. Press), 301
Meaburn, J. 1980, MNRAS, 192, 365
Nidever, D. L., Majewski, S. R., & Butler Burton, W. 2008, ApJ, 679, 432
Pathak, A., Pradhan, A. C., Sujatha, N. V., & Murthy, J. 2011, MNRAS, 412, 1105
Peeples, M. S., Werk, J. K., Tumlinson, J., et al. 2014, ApJ, 786, 54
Pellegrini, E. W., Oey, M. S., Winkler, P. F., et al. 2012, ApJ, 755, 40
Pietrzyński, G., Gieren, W., Graczyk, D., et al. 2013, in IAU Symp. 289, Advancing the Physics of Cosmic Distances, ed. R. de Grijs (Cambridge: Cambridge Univ. Press), 169
Putman, M. E., Bland-Hawthorn, J., Veilleux, S., et al. 2003, ApJ, 597, 948
Reid, W. A., & Parker, Q. A. 2012, MNRAS, 425, 355
Richter, P., de Boer, K. S., Werner, K., & Rauch, T. 2015, A&A, 584, L6
Richter, P., Fox, A. J., Wakker, B. P., et al. 2013, ApJ, 772, 111
Rosado, M., Laval, A., Boulesteix, J., et al. 1990, A&A, 238, 315
Salem, M., Besla, G., Bryan, G., et al. 2015, ApJ, 815, 77
Schwartz, C. M., & Martin, C. L. 2004, ApJ, 610, 201
Smart, B. M., Haffner, L. M., Barger, K. A., Hill, A., & Madsen, G. 2019, ApJ, 887, 16
Smoker, J. V., Fox, A. J., & Keenan, F. P. 2015, MNRAS, 451, 4346
Staveley-Smith, L., Kim, S., Calabretta, M. R., Haynes, R. F., & Kesteven, M. J. 2003, MNRAS, 339, 87
Tufte, S. L. 1997, PhD thesis, Univ. Wisconsin-Madison
Tumlinson, J., Thom, C., Werk, J. K., et al. 2011, Sci, 334, 948
van der Marel, R. P., & Kallivayalil, N. 2014, ApJ, 781, 121
van der Marel, R. P., Kallivayalil, N., & Besla, G. 2009, in IAU Symp. 256, The Magellanic System: Stars, Gas, and Galaxies, ed. J. T. Van Loon & J. M. Oliveira (Dordrecht: Kluwer), 81
Veilleux, S., Cecil, G., & Bland-Hawthorn, J. 2005, ARA&A, 43, 769
Wakker, B., Howk, J. C., Chu, Y.-H., Bomans, D., & Points, S. D. 1998, ApJL, 499, L87
Walker, A. 1999, ASSL, 237, 125
Werner, K., & Rauch, T. 2015, A&A, 584, A19
Winkler, P. F., Smith, R. C., Points, S. D. & MCELS Team 2015, in ASP Conf. Ser. 491, The Interstellar Medium in the Small Magellanic Cloud: Results from MCELS, ed. S. Points & A. Kunder (San Francisco, CA: ASP), 343